



1 **A versatile spaceborne architecture for immediate monitoring of the** 2 **global methane pledge**

3
4 Yuchen Wang¹, Xvli Guo¹, Yajie Huo¹, Mengying Li², Yuqing Pan^{1*}, Shaocai Yu^{2*}, Alexander
5 Baklanov³, Daniel Rosenfeld⁴, John H. Seinfeld⁵, and Pengfei Li^{1*}
6

7 ¹College of Science and Technology, Hebei Agricultural University, Baoding, Hebei 071000, P.R. China

8 ²Research Center for Air Pollution and Health; Key Laboratory of Environmental Remediation and Ecological Health,
9 Ministry of Education, College of Environment and Resource Sciences, Zhejiang University, Hangzhou, Zhejiang 310058,
10 P.R. China

11 ³Science and Innovation Department, World Meteorological Organization (WMO), Geneva, Switzerland

12 ⁴Institute of Earth Science, The Hebrew University of Jerusalem, Jerusalem, Israel

13 ⁵Division of Chemistry and Chemical Engineering, California Institute of Technology, Pasadena, CA 91125, USA
14

15 *Correspondence to: Pengfei Li (lpf_zju@163.com)

16 Shaocai Yu (shaocaiyu@zju.edu.cn)

17 Yuqing Pan (panyuqing@hebau.edu.cn)
18
19
20
21
22
23
24
25
26
27
28
29

30 *Submitted to*

31 *Atmospheric Chemistry and Physics*



32 **Abstract.**

33 The global methane pledge paves a fresh, critical way toward Carbon Neutrality. However, it remains largely invisible and
34 highly controversial due to the fact that planet-scale and plant-level methane retrievals have rarely been coordinated. This has
35 never been more essential within a narrow window to reach the Paris target. Here we present a versatile spaceborne architecture
36 to address this issue. Using this framework, we patrol the world, like the United States, China, the Middle East, and North
37 Africa, and simultaneously uncover methane-abundant regions and plumes. These include new super-emitters, potential
38 leakages, and unprecedented multiple plumes in a single source. More importantly, this framework is shown to challenge
39 official emission reports that possibly mislead estimates from global, regional, to site scales, particularly by missing super-
40 emitters. We reveal that this framework can enable ready-made satellites to initiate monitoring of the global methane pledge
41 immediately and is also versatile for upcoming stereoscopic measurements and artificial intelligence techniques.



42 1. Introduction

43 Global methane pledges finalized at the COP26 (the 26th United Nations Climate Change Conference of the Parties) have
44 been never more ambitious (Schellnhuber et al., 2016; Schurer et al., 2018; United Nations, 2021). More than 100 countries
45 have promised 30% methane emission reductions by 2030. Also, energy giants (e.g., Shell and BP) have committed to clear
46 targets of methane mitigation. Such pledges have never been more essential within a narrow window (< ten years) to reach the
47 Paris target. The scientific context is that atmospheric methane is a powerful greenhouse gas second only to carbon dioxide
48 (CO₂), trapping ~ 80 times more heat than the same amount of CO₂ (per molecule) over a 20-year time horizon (Etminan et
49 al., 2016; Saunio et al., 2016, 2020). Worse still, it is thought to rise since 2007 (Mikaloff and Hinrich, 2019), surge since
50 2014 (Nisbet et al., 2019), and set another record in 2021 (National Oceanic and Atmospheric Administration, 2022).
51 Fortunately, methane is short-lived (~ ten years) (K. et al., 2013) and can be reduced in half using existing technologies (Ocko
52 et al., 2021).

53 However, a classic dilemma emerges, dimming the hopes of scientists and policymakers (Masood and Tollefson, 2021). That
54 is, on the eve of the Paris target, those targets and emissions remain largely invisible worldwide and thus hinder effective
55 mitigation. The main issue is the Paris framework relies on countries or corporate giants to report emissions (A. et al., 2018,
56 2015; Ganesan et al., 2019). Moreover, the reports are based on indirect statistics, such as O&G inventories, rather than direct
57 measurements (Deng et al., 2022). This leads to a broad consensus that prominent discrepancies exist between the reports. For
58 example, field campaigns nearly double official claims of methane emissions in the United States by correcting leak
59 detection (A. et al., 2018).

60 To this end, widespread super-emitters present a unique opportunity worldwide (Duren et al., 2019; Pandey et al., 2019; T. et
61 al., 2022; Zavala-Araiza et al., 2015, 2017). They are typically responsible for the underestimates of methane emissions
62 (Alvarez et al., 2018; Duren et al., 2019; Itziar et al., 2021; T. et al., 2022; Thompson et al., 2016). Moreover, there is increasing
63 evidence that methane emissions follow a heavy-tailed distribution (Duren et al., 2019; Frankenberg et al., 2016; T. et al.,
64 2022), for which relatively small number of sources (so-called super-emitters) can account for a disproportionately large share
65 of total emissions. In contrast to area sources (e.g., cities), super-emitters are typically coal mines, wells, gathering stations,
66 storage tanks, pipelines, and flares, with even less than dozens of metres in diameter but high-concentrated methane plumes
67 (Allen et al., 2013; Miller et al., 2019; Subramanian et al., 2015; Varon et al., 2019). We thus anticipate that significant
68 emission mitigation could be achieved by deploying well-designed systems to identify methane super-emitters. For instance,
69 in support of the Paris agreement, the 17th World Meteorological Congress (2015) requested an Integrated Global Greenhouse
70 Gas Information System (IG3IS) that aimed to develop a measurement framework for methane emission reductions (Phil
71 DeCola and WMO Secretariat, 2017).

72 To date, a large body of field measurements (e.g., in situ and aircraft surveys) between 2012 and 2020 has been designed for
73 methane super-emitters. Despite this, they are spatially confined (e.g., regionally) and temporally infrequent (e.g., a few weeks),
74 incapable of exploring global methane super-emitters (A. et al., 2018; Conley et al., 2016; Duren et al., 2019; Marchese et al.,



75 2015; Nisbet et al., 2020; Smith et al., 2017; Thompson et al., 2016; Thorpe et al., 2016). Today, substantial advances have
76 been made towards detecting and quantifying methane super-emitters from space (Cusworth et al., 2019; Hu et al., 2018; Itziar
77 et al., 2022; Jacob et al., 2016; Pandey et al., 2019; Thompson et al., 2016). Such advances, however, have rarely been expanded
78 to measure the global methane pledge because large-scale swath and high-resolution sampling have not been coordinated. First,
79 global methane monitoring has become possible. A flagship satellite mission is the TROPOspheric Monitoring Instrument
80 (TROPOMI) onboard the Copernicus Sentinel-5 Precursor satellite (T. et al., 2022; Veefkind et al., 2012). It can offer daily
81 global insights for methane column concentrations, with a large swath width of ~ 2600 km, a moderate resolution of 7.0×5.5
82 km^2 (since August 2019), and high signal-to-noise ratios. However, its relatively coarse spatial sampling still limits its
83 application to detect methane super-emitters (T. et al., 2022). Second, next-generation satellite missions, pioneered by the
84 GHGSat constellation (three satellites at the moment), emerge for mapping methane super-emitters (Cusworth et al., 2019),
85 with a narrow swath (e.g., ~ 12 km) but a ground-breaking high-resolution spatial sampling (e.g., $25 \sim 50$ m)(Jervis et al., 2021;
86 Varon et al., 2020). Complementary to the GHGSat constellation, satellite-based hyperspectral imager spectrometers, such as
87 PRISMA, Gaofen-5, ZY1, Sentinel-2, and Worldview-3, have shown great potentials (Guanter et al., 2021; Itziar et al., 2021;
88 Sánchez-García et al., 2021; Varon et al., 2021). They can resolve methane enhancements and attribute them to specific
89 infrastructures via similar narrow swath and high-resolution sampling (e.g., 30 m). Note that regions those satellites usually
90 gazed at are originally well-known home to methane super-emitters. Narrow swath coverage thus remains a crucial limitation
91 for global surveys of methane super-emitters. Collectively, existing satellite missions still lack both global vision and keen
92 insight and thus cannot sustain the global methane pledge.

93 Here we present a multi-tiered, space-based framework for global-scale and high-resolution methane retrievals. The key is that
94 ready-made satellite missions alone have the potential to initiate immediate monitoring of the global methane pledge. Using
95 this framework, we patrol the world, with an experimental focus on China, the United States, Iraq, Kuwait, and Algeria, and
96 reveal both region-scale hotspots and plant-level super-emitters. We can even gaze at a single source to map multiple plumes
97 and inspect possible methane leakages. These results can challenge national reports that possibly miss unexpected super-
98 emitters or mislead emission magnitude. On the eve of the Paris target, at least while a global methane monitoring network is
99 not in place, this multi-tiered satellite constellation presented in this study has important implications for measuring global
100 methane pledges. Further information on methane retrievals and emission estimates, as well as uncertainty analysis, are shown
101 in Materials and Methods.

102 **2. Materials and Methods**

103 **2.1 Multi-tiered satellite constellation**

104 The multi-tiered satellite constellation was designed to reconcile global-scale and high-resolution methane monitoring. First,
105 TROPOMI offered a unique potential for global methane monitoring, depending on its large-scale (i.e., 2600 km) swath, daily
106 revisit time, regional footprint (i.e., $5.5 \times 7 \text{ km}^2$ since August 2019), and sounding precision and accuracy (i.e., $< 1\%$)



107 (Veefkind et al., 2012). Approximately, TROPOMI observed a full swath per second, which resulted in ~ 216 spectra per
108 second. This instrument comprised two spectrometer modules, the first involving near-infrared (NIR) spectral channels, and
109 the second dedicated to the shortwave-infrared (SWIR) spectral channel. The NIR and SWIR channels were equipped with
110 spectral resolutions of 0.38 and 0.25 nm and spectral sampling ratios of 2.8 and 2.5, respectively. Since the NIR and SWIR
111 detectors are incorporated in different instrument modules, the NIR spectra will be co-registered with the SWIR spectra before
112 performing methane retrievals. The methane total column-averaged dry-air mole fraction (X_{CH_4}) is retrieved from near-
113 infrared (NIR) (757 ~ 774 nm) and shortwave-infrared (SWIR) (2305 ~ 2385 nm) spectral measurements for sunlight
114 backscattered by Earth's surface and atmosphere (Hu et al., 2018). In this study, only high-quality measurements, retrieved
115 under cloud-free and low aerosol load conditions, were used. These measurements were filtered, in addition, for solar zenith
116 angle ($< 70^\circ$), low viewing zenith angle ($< 60^\circ$), and smooth topography (the surface elevation of < 80 m within 5 km radius)
117 as described in Hu et al. (28) (Hu et al., 2018).

118 Hyperspectral satellite missions severed as the second tier, responsible for mapping localized methane super-emitters
119 depending on their unprecedented resolution (i.e., 3m ~ 50m). Therein PRISMA, as an open-access representative, was
120 specifically suitable for this work. It can image the solar radiation reflected by the Earth's surface and atmosphere via hundreds
121 of spectral channels between the visible and SWIR spectrum (~ 400 ~ 2500 nm). Measurements in the SWIR spectrum from
122 2000 to 2500 nm sampled absorption features from water vapor, carbon dioxide, and methane. Therein the 2100 nm and 2450
123 nm windows were especially sensitive to methane. Furthermore, the signal-to-noise ratio was reported to be about 100 in the
124 SWIR for a relatively dark vegetation pixel and increased to above 200 for bright soil surfaces in oil and gas extraction sites.
125 More importantly, it covered areas of 30×30 km² with a 30 m spatial sampling.

126 We collected dozens of daily measurements from the multi-tiered satellite constellation. These measurements experimentally
127 mapped regional methane hotspots and localized methane super-emitters across the United States, China, the Middle East (Iraq
128 and Kuwait), and North Africa (Algeria). The acquisitions were mostly taken between April 2020 and January 2022.

129 **2.2 Multi-tiered methane retrievals**

130 In the first tier of our framework, we employed the operational methane products via TROPOMI onboard the Sentinel 5 satellite.
131 The target product was the column-averaged dry-air volume mixing ratio of methane (X_{CH_4}), which will be retrieved
132 simultaneously with scattering properties of the atmosphere. The operational retrieval algorithm is based on RemoTeC (Butz
133 et al., 2009; Hasekamp and Butz, 2008), which was originally developed for CO₂ and methane retrievals from GOSAT
134 observations (Butz et al., 2011). It attempted to fit spectra observed by the TROPOMI-based NIR and SWIR channels. Its
135 sensitivities to atmospheric scattering properties, atmospheric input data, and instrument calibration errors had been
136 extensively evaluated (Sha et al., 2021; Verhoelst et al., 2021). As a result, the operational products were proved to be critically
137 stable, with a convergence rate of 99%, and high significance by comparisons with both satellite-based (e.g., GOSAT) and
138 ground-based (e.g., TCCON) measurements. The required accuracy and precision of < 1 % for the X_{CH_4} product were met
139 for clear-sky measurements over land surfaces and after appropriate filtering of difficult scenes. Moreover, the forward model



140 error was less than 1 % for about 95 % of the valid retrievals. Model errors in the input profile of water did not influence the
141 retrieval outcome noticeably. The methane product is expected to meet the requirements if errors in input profiles of pressure
142 and temperature remain below 0.3% and 2 K, respectively. Of all instrument calibration errors, the retrieval results were the
143 most sensitive to an error in the instrument spectral response function of the shortwave infrared channel.

144 To achieve long-term (i.e., one year) methane retrievals, we oversampled the TROPOMI data at 5×5 km² resolution following
145 Sun et al. (2018) (Sun et al., 2018) where the full spatial footprint of the observation was taken into account by attributing the
146 observed value to grid cells weighted by the spatial overlap of the observation with those grid cells.

147 In the second tier of our framework, we applied the matched-filter algorithm to calculate per-pixel methane enhancements with
148 respect to background levels based on the SWIR sample spectrum (i.e., the 2100 - 2450 nm window) onboard the PRISMA
149 (Foote et al., 2020; Guanter et al., 2021; Itziar et al., 2021). In theory, the retrieval method can depend on physically-based or
150 data-driven algorithms. The former aims to explicitly resolve the radiative transfer between the surface, the atmosphere, and
151 the hyperspectral spectrometers. A key representative is the family of differential optical absorption spectroscopy (DOAS)
152 methods (Cusworth et al., 2019, 2020, 2021b, 2021a). The latter seeks a methane absorption spectrum across a hyperspectral
153 image using statistical methods. It is commonly based on the matched-filter and the singular vector decomposition concepts.
154 These methods are both widely applied and evaluated, especially onboard satellite (e.g., PRISMA, GF-5, and ZY-1) and
155 airborne (e.g., AVIRIS and AVIRIS-NG) platforms (Cusworth et al., 2020; Foote et al., 2020; Guanter et al., 2021; Itziar et
156 al., 2021; Thompson et al., 2016; Thorpe et al., 2016).

157 In this study, the data-driven retrieval based on the matched-filter concept was used. The main reason was that it could
158 implicitly account for potential radiometric and spectral errors in satellite-based imaging spectroscopy. For instance, vertical
159 striping was prevalent in hyperspectral measurements due to detector inhomogeneity, thus substantially degrading methane
160 retrievals. The matched-filter algorithm focused on the per-pixel columns and thus tackled this issue in principle. Besides, the
161 physically-based method had to consider background concentrations that were difficult to determine around the super-emitters.
162 In contrast, the data-driven method was independent of background levels and can directly seek methane enhancements. Finally,
163 the data-driven method generally had a substantially superior computational efficiency compared to the physically-based
164 method.

165 The matched-filter retrieval used here was similar to the one used by Thompson et al. (2016) (Thompson et al., 2016) for the
166 Hyperion imaging spectrometer onboard the EO-1 satellite. The calculation processes of methane enhancements ($\Delta \mathbf{XCH}_4$,
167 **ppb**) were as follows.

168
$$\Delta \mathbf{XCH}_4(\vec{\mathbf{x}}) = \frac{(\vec{\mathbf{x}} - \vec{\boldsymbol{\mu}})^T \boldsymbol{\Sigma}^{-1} \vec{\mathbf{t}}}{\vec{\mathbf{t}}^T \boldsymbol{\Sigma}^{-1} \vec{\mathbf{t}}} \text{ (Eq. 1)}$$

169 The $\vec{\mathbf{x}}$ denoted the spectrum under analysis. The $\vec{\boldsymbol{\mu}}$ and $\boldsymbol{\Sigma}$ represented the mean background radiance and corresponding
170 covariance, respectively. They were calculated based on per-column spectrums in order to consider different responses of
171 across-track detectors to radiance. The $\vec{\mathbf{t}}$ was the target spectrum that reflected the background radiance enhanced by the
172 methane plume. It was generated by the elementwise multiplication of $\vec{\boldsymbol{\mu}}$ and $\vec{\mathbf{k}}$. This implicit parameter $\vec{\mathbf{k}}$ represented a unit



173 methane absorption spectrum derived from a look-up table simulated by the MODTRAN radiative transfer model. Similarly,
174 the spectral convolution was also performed on a per-column basis.

175 In theory, methane enhancements detected in spectrometers generally exhibit sparsity, especially over low albedo surfaces.
176 We thus accounted for such non-specificity effects to improve the basic version of the matched-filter model. A major measure
177 to compensate for the albedo effect was to scale the target spectrum \vec{t} by the pixel-specific albedo factor due to the fact that
178 the Beer–Lambert absorption law depended on the initial radiance in the absence of the absorber. Here the pixel-specific scalar
179 f was calculated based on the spectral average $\vec{\mu}$ and the analysis spectrum \vec{x} as follows:

$$180 \quad f = \frac{\vec{x}^T \vec{\mu}}{\vec{\mu}^T \vec{\mu}}. \text{ (Eq. 2)}$$

181 This solution made ΔXCH_4 normalized by the albedo term, which was similar to the per-pixel normalization in previous
182 hyperspectral analysis (Kraut et al., 2005).

183 The premise to launch the matched-filter algorithm was the accurate knowledge of the response of the instrument spectra to
184 the methane absorption nature. To this end, the objective was to gain the best fit between the simulated and reference spectra.
185 An initial step was thus conducted to update the spectral calibration for the channels within the 2100 - 2400 nm window, in
186 which the channel wavelength centre and width were updated for each across-track position in each scene. Other details are
187 illustrated in previous attempts (Foote et al., 2020; Guanter et al., 2021; Itziar et al., 2022).

188 **2.3 Multi-tiered attribution of methane hotspots and plumes**

189 In the first tier of our framework, we filtered the TROPOMI-based methane retrievals to identify region-scale hotspots. In each
190 scene, we focused on the grids with anomalous values that were noticeably higher than the average. In this study, we used a
191 Boolean mask to define the pixels that were affected by the methane emissions (Pandey et al., 2019). Although automatic
192 threshold and algorithm might result in more consistent and flexible identifications, no satisfactory set of criteria was found
193 that could be applied for this study. This was mainly because, in localized regions, the methane budgets responded to the
194 changes in not only the super-emitters but also the background. Assisted by artificial intelligence techniques in the future
195 (Ouerghi et al., 2021; Paoletti et al., 2018; Yang et al., 2018; Yu et al., 2017; Zhang et al., 2018), our framework can derive a
196 global, operational, and open-access methane monitoring network. As expected, multiple hotspots of interest result, and here
197 we focused on those in the United States, China, Iraq, Kuwait, and Algeria.

198 In the second tier of our framework, we applied visual inspection to detect plumes using the PRISMA-based methane retrievals
199 (Itziar et al., 2021; Martin et al., 2018; T. et al., 2022; Varon et al., 2020). To date, it was still challenging to distinguish
200 methane plumes in hyperspectral images using full physically-based algorithms. The main cause was potential methane
201 retrieval artifacts from hyperspectral satellites that were spatially correlated to surface features. Specifically, we manually
202 searched for methane enhancement pixels with gas-plume-like shapes, i.e., high methane enhancements progressively
203 decreased downwind. The resulting pixels were subsequently compared to the spectral radiance data at the 2300 nm absorption
204 feature sensitive to low surface albedos. In this way, the fake positives due to specific surface features were prevented. On this



205 basis, the candidate pixels were overlaid over simultaneous (i.e., hourly) wind fields and high-resolution imageries in
206 individual scenes. They would be considered to be true plumes if they roughly aligned with simultaneous wind direction and
207 originated from explicit infrastructures. Here the high-resolution satellite imageries were taken from the Google Map. The
208 hourly wind field data came from the ERA5 reanalysis dataset produced by the European Centre for Medium-Range Weather
209 Forecasts (ECMWF) (Hersbach et al., 2020; Hoffmann et al., 2019). Finally, we manually drew polygons to mask such
210 resulting plumes out. As preparation for plume emission quantification, we removed the background using the threshold of the
211 median values of the scenes.

212 These satellite imageries allowed us to categorize methane plumes within narrow spatial scales between 50 to 500 m², such as
213 O&G extraction platforms, storage tanks, and compressor stations. They even enabled the attribution of plumes to specific
214 emission ports in individual sources due to their very high resolution. Furthermore, we could name them based on points of
215 interest in the Google Map. On this basis, such sources could be visually retrospectively via long-term, high-resolution (i.e., 10
216 m) satellite images from the Sentinel-2 mission (Ehret et al., 2021; Varon et al., 2021). Their key details, like ages and statuses
217 (e.g., active or inactive), were thus collected reliably. Note that, regarding such information, national reports were typically
218 credible but inaccessible, particularly in global missions. In addition, it should be highlighted that, on top of considerably high
219 budgets, like megacities, there must be super-emitters undetectable in our way. Other causes are discussed in uncertainty
220 analysis in Supplement Information.

221 2.4 Multi-tiered quantification of methane emissions

222 In our framework, we calculated the total excess mass of methane in kilograms in the detected hotspots (in the first tier) and
223 plumes (in the second tier) using the so-called integrated mass enhancement (IME) model (Frankenberg et al., 2016; Varon et
224 al., 2018). To make conservative estimates, we defined the background levels as the 10% of the average methane
225 concentrations in the TROPOMI-based and PRISMA-based scenes (Figs. 1b ~ 1g) (Frankenberg et al., 2016; Varon et al.,
226 2018). On this basis, we eliminated the interferences from the background concentrations and calculated IMEs as the methane
227 masses of the masked hotspots and plumes.

228 Overall, this method linked the emission rate (Q) with the measured IME via the residence time of methane (IME/Q). This
229 residence time relied on an effective wind speed (U_{eff}) and a characteristic plume size (L) as follows:

$$230 \quad Q = \frac{U_{\text{eff}} \cdot \text{IME}}{L}. \quad (\text{Eq. 3})$$

231 Specifically, the IME and L can be inferred from the observations of the hotspots or plumes. During this process, we carefully
232 applied a Boolean plume mask that separated the pixels (i) with notable signals ($\Delta\Omega_i$) from background pixels and thus defined
233 the total areas ($\sum_{i=1}^N A_i$) of the hotspots or plumes. The L was defined as the square root of the total plume areas. Hence, the
234 IME was calculated as follows:

$$235 \quad \text{IME} = \sum_{i=1}^N \Delta\Omega_i A_i. \quad (\text{Eq. 4})$$



236 In the first tier of our framework, the effective wind speed (U_{eff}) was defined as the 10-m wind speed U_{10} obtained from the
237 ERA5 reanalysis dataset. According to the detected hotspot, the value at the nearest hour and location were used.

238 In the second tier of our framework, we applied an ensemble of large eddy simulations (LES) to establish an empirical, linear
239 relationship between U_{eff} and the measured 10-m wind speed U_{10} as follows (Fig. S9)

240 $U_{\text{eff}} = 0.8602 \ln(U_{10}) + 1.1513$. (Eq. 5)

241 The configurations of these simulations, such as spatial resolution and precision, were comparable to our PRISMA data. Other
242 details in this methodology were described in Varon et al. (2018) (Varon et al., 2018).

243 We estimated the uncertainties of Q by propagating the random errors in U_{10} and IME . This processes were conducted in
244 previous studies (Cusworth et al., 2019, 2021b; Itziar et al., 2021). As shown in previous findings, the major error source came
245 from the U_{10} term. Its random distributions typically corresponded to the 50% random error. On this basis, this error was
246 integrated quadratically with the standard error of the IME , the result of which can be treated as the final random error of Q .

247 The intrinsic errors of the IME model were quantified in the following uncertain analysis.

248 2.5 Uncertainty Analysis

249 The objective of this work was to promote a multi-tiered satellite constellation that can monitoring global methane pledges.
250 To better understand the performance of our framework, we conducted comprehensive uncertain analysis. Note that the
251 protocol of the uncertain analysis on our framework originated from previous studies (Itziar et al., 2021; Varon et al., 2020).
252 Specifically, we required to account for the uncertainties in the TROPOMI-based and PRISMA-based methane retrievals and
253 subsequent emission estimates. Therein the operational TROPOMI-based methane retrieval products had been evaluated
254 strictly and proved to be reliable globally (except in low- and high-albedo and snow-covered areas) (Lorente et al., 2021; Sha
255 et al., 2021). In this work, we thus focused on three main sources of uncertainties, specifically including (1) uncertainties in
256 the PRISMA-based methane retrievals; (2) uncertainties in the TROPOMI-based methane emission estimates; and (3)
257 uncertainties in PRISMA-based methane emission estimates. During the analysis for the latter two uncertain sources, we would
258 further investigate the potential wind impacts on the methane emission estimates. Note that it remained challenging to directly
259 quantify the uncertainties in the wind fields across our cases due to the lack of measurements. We would thus assess the
260 variations in the methane emission estimates driven by distinct wind data. From such analysis, we could confirm the reliable
261 performance of our framework. Details can be found in Supplementary Information.

262 3 Results and discussions

263 3.1 Multi-tiered imaging of global methane hotspots and super-emitters

264 Figure 1 presents representative sets of methane hotspots and associated super-emitters across the United States, China, the
265 Middle East (Iraq and Kuwait), and North Africa (Algeria) via our multi-tiered satellite constellation. Each group first clarified



266 a methane-abundant region and further focused in on explicit super-emitters. Among them, five methane-abundant regions
267 were captured in Wattenberg (the United States), Yangquan (China), Rumaila (Iraq), Burgan (Kuwait), and Hassi Messaoud
268 (Algeria) (Fig. 1a and Table S1). These accounted for 4805 ~ 46138 kg/h methane emissions based on our daily first-tiered
269 (i.e., TROPOMI-based) monitoring. From the perspective of a state-of-the-art global methane emission inventory (i.e.,
270 EDGARv6.0), such high values ranked among the top 1% regarding emission intensities per unit area (km²) (Fig. S1)(Crippa
271 et al., 2020). The Rumaila field, for example, was known as the largest oil field in Iraq (in terms of both reserves and yields).
272 In this work, it was found with a significant methane emission intensity exceeding 45000 kg/h (Fig. 1b). In addition to such
273 well-known oil fields (Figs. 1c ~ 1f), methane hotspots emerged in developing coal mines, like Yangquan, with comparable
274 emission levels (> 30000 kg/h) (Fig. 1g).

275 We attributed these methane enhancements to specific methane plumes via the second-tiered (i.e., PRISMA-based) monitoring
276 (Figs. 1b1 ~ 1g2). There are substantial variations in the methane plumes' amounts, types, and magnitude, even in a single
277 methane-abundant region. For instance, in the Burgan field, the second-tiered monitoring detected up to eight methane plumes
278 in a handful of grids in the first-tiered monitoring (Figs. 1c1 ~ 1c4 and 1d1 ~ 1d4). Such intensive distributions were also
279 found in previous region-oriented surveys in the Permian basin and California (Duren et al., 2019; Itziar et al., 2021). Together
280 with high-definition images (Fig. S2), we found that such plumes originated from various sources, such as flares, factories,
281 and wells. A breakthrough was the capture of two distinctive plumes in an individual methane source with extremely high
282 emissions (> 10000 kg/h), unprecedented in previous satellite-based exploration and only observable in aircraft surveys (Fig.
283 1b1). Such precise distinction benefited from the high resolution of the second-tiered monitoring, despite being limited by the
284 relatively higher detection threshold (~ 300 kg/h) (Guanter et al., 2021). Besides, factories and wells can also emit such evident
285 plumes (Fig. 1c1 and Figs. 1e1 and 1e2). By comparison, other plumes were typically more diffuse but with comparable
286 emission magnitude (~ 1000 ~ 7000 kg/h).

287 Note that the above results represent only snapshots at the overpass moments of the satellites (i.e., TROPOMI and PRISMA)
288 (Figure 1). Specifically, for a given set (including both a methane-abundant region and associated super-emitters), the overpass
289 timing of TROPOMI can be nearly concordant with that of PRISMA. The temporal gaps could be frequently controlled within
290 ten days (e.g., Figs. 1b and 1d), even two days (Figs. 1e, 1f, and 1g). For instance, within only two days (August 18th and 19th,
291 2021, November 15th and 17th, 2021), our multi-tiered satellite constellation went through the Hassi Messaoud field and the
292 Yangquan coal mine and provided in-depth views of methane budgets, including methane-abundant regions and their drivers
293 (Figs. 1e and 1g). Even, in just one day (July 7th, 2021), our multi-tiered satellite constellation not only uncovered methane
294 enhancements in the Wattenberg field (Fig. 1f) but also tracked them back to explicit methane super-emitters (Figs. 1f1 and
295 1f2). As expected, if we extended the monitoring window of our framework to years, more methane super-emitters were
296 subsequently captured (Figs. S3 and S4). Moreover, our framework via multi-tiered satellite constellation paves an in-time
297 way for routine monitoring of global methane hotspots and associated super-emitters.



298 **3.2 Multi-tiered verification of global methane super-emitters**

299 Four unexpected cases occurred in Burgan (Iraq), Hassi Messaoud (Algeria), and Yangquan (China), potentially explainable
300 if we took mutual verification of the first- and second-tiered monitoring into consideration. First, an anomalous methane plume
301 was detected in the Burgan field (Fig. 1c4) of high emission magnitude (> 1500 kg/h), notably exceeding typical O&G facilities,
302 from an elusive source (i.e., no clear source could be attributed) (Fig. S2). The long-term measurements of our multi-tiered
303 satellite constellation intermittently, rather than accidentally, observed this abnormal plume (Figs. S4). Furthermore, uncertain
304 analysis (see Materials and Methods) helped confirm this real plume. In particular, the methane plumes were clearly
305 uncorrelated with the surface brightness from space (Fig. S5). Consequently, the most likely hypothesis for this super-emitter
306 was methane leakage from gigantic O&G pipelines as shown in the Google Map (Fig. S2).

307 Second, we observed suspect trails of methane plumes above the storage tanks in the Burgan field (Fig. 1d4). Conceivably, the
308 technical noise driven by albedo effects bore the brunt, although it was believed to be corrected reliably (See Materials and
309 Methods). To this end, we applied a multi-spectral retrieval algorithm to eliminate this effect to a large extent. The detailed
310 illustrations are shown in Materials and Methods (Fig. S6). Consequently, we provided evidence that un-negligible methane
311 emissions (> 3500 kg/h) may very well be the unique explanation, likely related to fugitive methane leaks from the storage
312 tanks. This was only seen in previous aircraft-based surveys (Frankenberg et al., 2016). Therefore, our multi-tiered outcomes
313 indicate even more widespread methane leaks than expected. Note that the multi-spectral retrieval algorithm cannot completely
314 remove the albedo effects on our framework. As such, our framework could lead to efficient on-site re-inspection on worldwide
315 and innumerable O&G fields.

316 Third, our framework detected a new methane super-emitter in the Hassi Messaoud field on December 7, 2021 (Fig. 1e4). By
317 revisiting historical satellite images in the second-tiered monitoring (Fig. S7), we could confirm that this super-emitter arose
318 between October 18th and November 12, 2021. These results indicate that monitoring of global methane super-emitters can
319 attain monthly resolution via current satellite constellation alone. Conceivably, more satellite observations would further close
320 the time window. Fourth, a distinct methane plume appeared in a coal mine in a mountainous area (Yangquan, China),
321 exceeding all of the detected O&G super-emitters regarding the emission rate (> 7000 kg/h) (Fig. 1g1).

322 Figure 2a illustrates that, in our multi-tiered satellite constellation, the extent to which the explicit plumes in the second tier
323 explained the regional budget detected by the first tier. Overall, the plumes in the former were mostly responsible for large
324 shares ($> 8.2\%$) of regional budgets in the latter. In the Rumaila, Burgan, and Wattenberg fields, the detected methane plumes
325 played a more critical role, with contributions up to $53.8 \sim 65.9\%$. Note that such contribution estimates might occasionally
326 exceed 100% mainly owing to the inconsistent overpass moments between the first- and second-tier monitoring. By
327 comparison, the relatively low but still significant contributions in the Hassi Messaoud field (8.2%) and Yangquan coal mine
328 (35.7%) were partly due to the technical limitation of our framework in detecting methane plumes on top of high background
329 levels. Collectively, the heavy-tail law of methane plume distributions, early reported for regional O&G fields (like the Permian
330 basin and California) (Duren et al., 2019; Itziar et al., 2021), possibly applied worldwide.



331 To further explore such a hypothesis, we extended the temporal sample window of our multi-tiered framework. As expected,
332 the first tier pictured less vivid methane enhancements mainly due to wind averages (Martin et al., 2018; McLinden et al.,
333 2016; Sun et al., 2018) (Fig. S3), while the second tier could capture more methane plumes (Fig. S4). This would lead to more
334 volatile contributions of the plumes to regional budgets, which, however, remained at high levels. This reinforces the above
335 hypothesis for the widespread occurrence of methane super-emitters.

336 A regional survey in a California field was considered as the best reference, owing to its utilization of systematic airborne
337 measurements to detect and quantify methane super-emitters (Duren et al., 2019). They survey reported 1181 methane plumes,
338 more than 500 times larger than previous aerial studies (Englander et al., 2018), with a median emission intensity of 170 kg/h.
339 These results were thus used to directly evaluate the outcomes in the second tier (Fig. 3). Even though some regions of interest
340 in this study were far less famous than the California field, their emission intensities were much higher. Specifically, these
341 plumes detected by the second-tiered monitoring had emission intensities (1142 ~ 11698 kg/h) that exceeded the median value
342 in the California field. Satellite-based surveys conducted repeatedly for the Permian basin (one of the top O&G bases
343 worldwide) from 2019 to 2020 (Fig. 3) as compared to the surveys in the California field, they achieved a much higher number
344 of strong methane super-emitters, the median emission rates (1850 kg/h) much closer to ours (2888 kg/h). Collectively, this
345 direct comparison indicates the outstanding strength of our results that, though derived from a small dataset, could be analogous
346 to abundant outcomes from field campaigns. More importantly, this highlights the urgent need for global monitoring of
347 'nameless' O&G facilities that possibly emit methane as much as the California field and Permian basin.

348 **3.3 Multi-tiered challenges of national emission inventories**

349 These multi-tiered results challenge traditional methane emission inventories (Fig. 4). Here the conventional emission data
350 was obtained from a state-of-the-art bottom-up emission inventory (i.e., EDGARv6.0) for the year 2018. Consequently, for
351 the methane hotspots, this inventory was mostly consistent with the present results (-49.9 ~ 91.8%), with a fine average bias
352 (63.2%). The Hassi Messaoud field in Algeria was a unique exception, where the O&G sector was in rapid development, with
353 a relatively larger bias (489.2%). By comparison, this inventory significantly undervalued the methane super-emitters (up to
354 orders of magnitude). This indicates that traditional emission inventories might have acceptable performance for traditional
355 methane-abundant regions while incapable of tracking methane super-emitters.

356 First, outdated spatial proxies might explain the large divergence between our plant-based estimates and the EDGARv6.0 (Fig.
357 1b1 and Fig. S8). Moreover, the EDGARv6.0 was designed for the year 2018, missing the newly established O&G plants with
358 high methane emissions. Second, in principle, conventional inventories directly missed high emissions caused by abnormal
359 operations (e.g., equipment failures) (Fig. 1c4 and Fig. S8) such as the O&G blowout shown in on-site surveys (Pandey et al.,
360 2019). A compromise was downwind measurements, yet insufficiently reliable as shown in previous findings (A. et al., 2018).
361 In addition, the relatively low bias in the Rumaila and Hassi Messaoud fields might be explained by other causes (Figs. 1b2
362 and 1e3) such as outdated emission factors. Empirically, a plant-level inventory, once optimized by direct measurements, can



363 raise total methane emissions by ~ 60%, although source categories vary substantially (A. et al., 2018). Besides, temporal
364 variability might also explain top-down and bottom-up differences in methane emission estimates. For instance, the peak
365 emission rate could exceed 40% higher than the average, which might occur in the middle afternoon due to specific processes,
366 like episodic venting from manual liquid unloading (Vaughn et al., 2018). This aligned with the sampling time of the satellites,
367 thus biasing bottom-up inventories. Collectively, it is necessary to carefully consider all factors affecting methane emissions,
368 including emission factor updating and spatiotemporal variations, in order to develop effective strategies for mitigating
369 methane emissions.

370 **3.4 Implications for global methane monitoring**

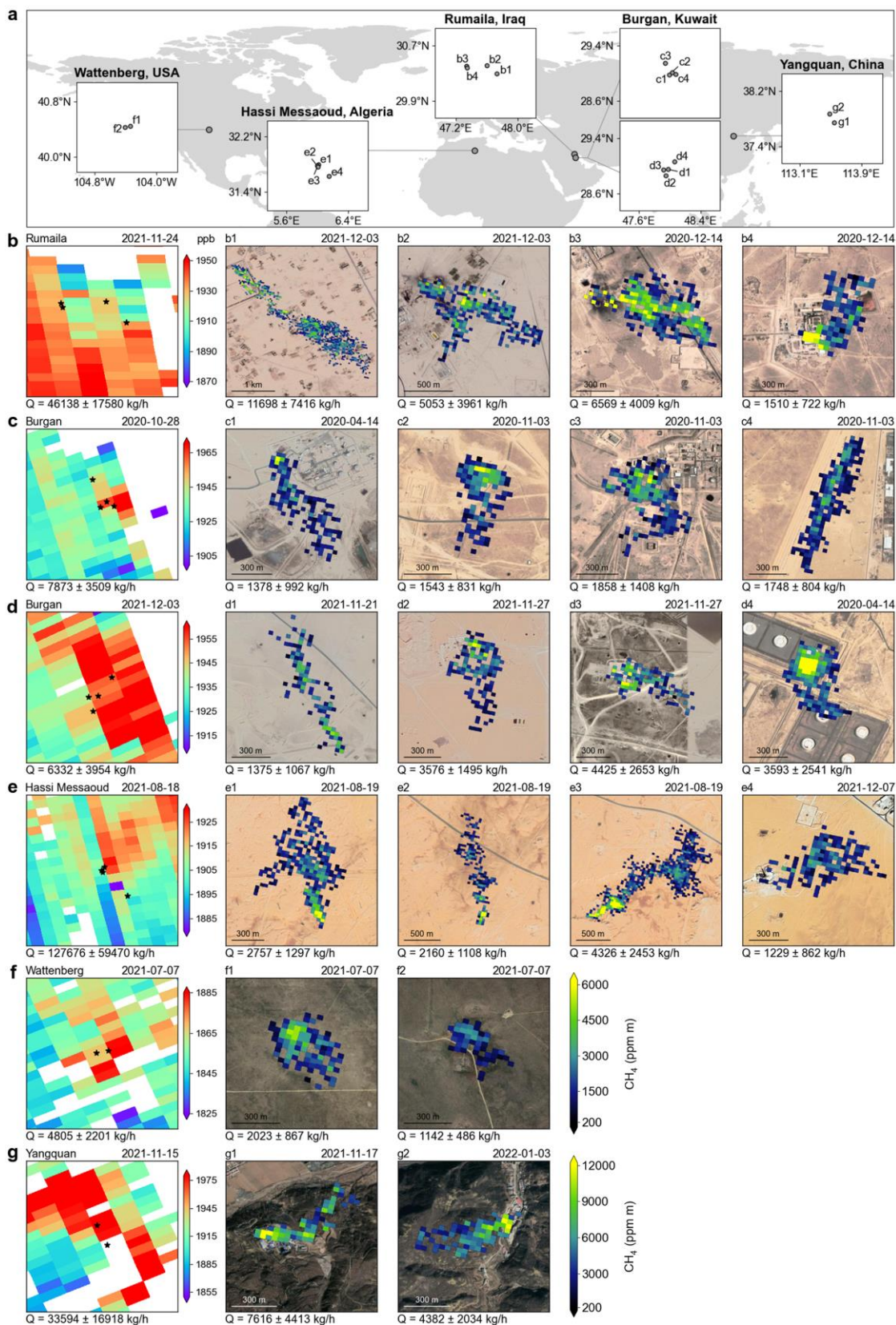
371 We present a multi-tiered, space-based framework that can harmonize planet-scale and plant-level methane retrievals (Fig. 5).
372 Using this framework, we patrol the world, with synergistic, proactive detections on the methane-abundant regions and
373 methane super-emitters across the United States, China, the Middle East (Iraq and Kuwait), and North Africa (Algeria). We
374 even lock new methane super-emitters, track potential methane leakages from storage tanks, and distinguish multiple methane
375 plumes in a single source. Such achievements are mostly unprecedented in satellite surveys and only observed in aircraft
376 campaigns. On this basis, our results challenge national reports that possibly miss unexpected super-emitters or mislead
377 emission magnitude, partly due to surges of oil and gas (O&G) facilities and widespread abnormal operations.

378 Our data prove that depending on ready-made satellite missions alone can initiate immediate, proactive monitoring of global
379 methane pledges, in contrast to existing surveys that have to focus on a priori methane-abundant regions. As such, as the
380 window for achieving the Paris target is rapidly closing, we will not need to sit back and wait for upcoming space missions,
381 like MethaneSAT and SBG in the United States, EnMAP in Germany, a new version of GF-5 in China, and, later, the European
382 Space Agency's CHIME from 2025 to 2030 (Cusworth et al., 2019). In addition, while scientific communities persistently
383 debates the drivers of the recent methane surge (G. et al., 2014; Nisbet et al., 2019; Turner et al., 2019), the consequences of
384 our outcomes are clear, not only holding clues but also facilitating mitigation.

385 It should be noted that the multi-tiered framework is sustainable (Fig. 5). On the one hand, it can harmonize multiple satellites.
386 The potential representatives include upcoming official missions (e.g., the GF-5) (Itziar et al., 2021), current private
387 constellations (e.g., the GHGSat series) (Jervis et al., 2021; Varon et al., 2020), and explorable multispectral products (e.g.,
388 the Worldview-3 and Sentinel-2) (Sánchez-García et al., 2021). On the other hand, the framework is not confined to satellites
389 and can be expanded by integrating in situ (e.g., Global Atmosphere Watch Programme) (World Meteorological Organization,
390 2022), aircraft, and unmanned aerial vehicles (UAVs) (Cusworth et al., 2020; Gålfalk et al., 2021; Tuzson et al., 2020).
391 Particularly, on the basis of our framework, rapid advances in artificial intelligence (AI) techniques are projected to completely
392 replace manpower to seek faint signals of methane enhancements in Earth's surface, and to significantly optimize data-driven
393 algorithms of methane emission estimates (Reichstein et al., 2019; Yuan et al., 2020). In principle, subsequent mitigation of

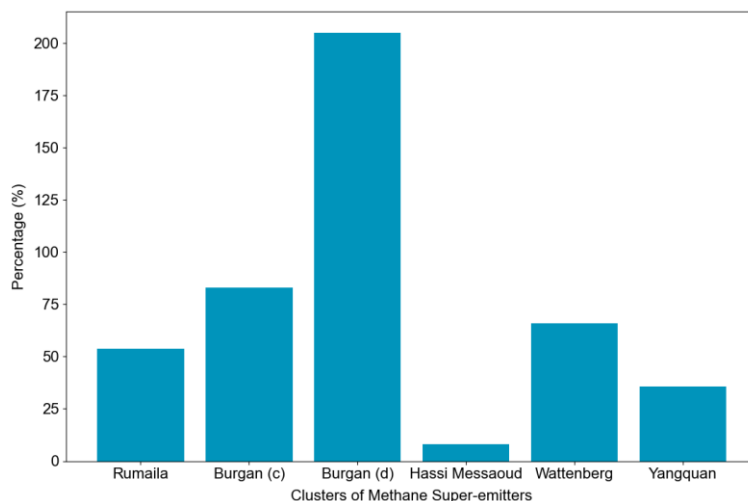


394 such super-emitters via routine maintenances, leak detections, or emergent repairs can provide effective, efficient, and
395 economical solutions toward the Paris target (Mayfield et al., 2017).
396 These outcomes have important ramifications for low- and middle-income countries. World powers, like the United States and
397 European Union, lead new national methane pledges. They are separately on the way to creating vast operational infrastructures
398 to monitor ambitious climate goals. Still, huge holes remain in coverage and authority, at least by the middle of this decade.
399 This situation is especially worse for low- and middle-income countries, where the tight budget dims the hopes for filling up
400 those holes by 2030, while methane emissions are likely to rise as countries develop. In this context, the present framework
401 can at once serve as the cost-effective piece of the global methane monitoring network and thus support fair climate
402 negotiations between countries.
403



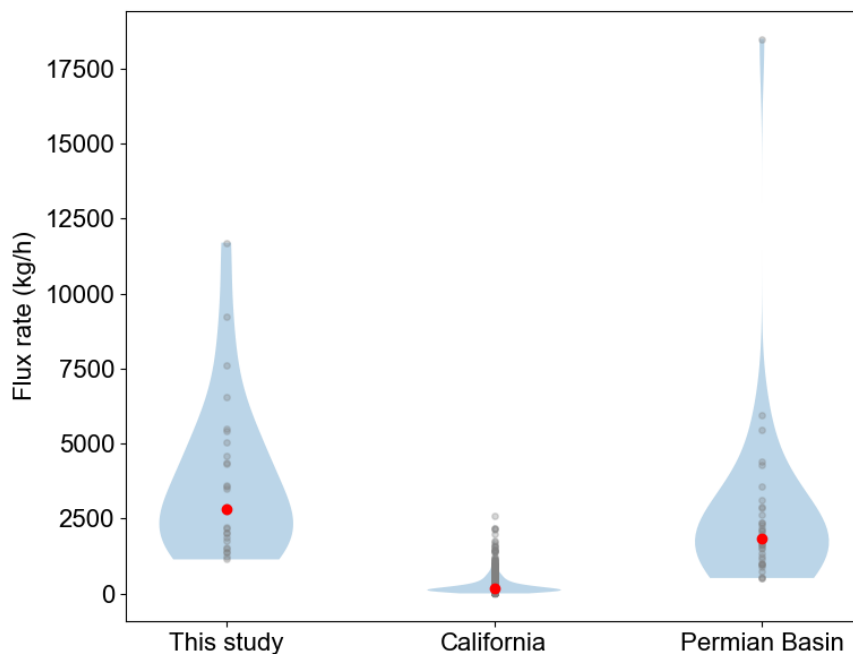


405 **Fig. 1. Methane hotspots and associated super-emitters across the United States, China, Iraq, Kuwait, and Algeria via**
406 **the multi-tiered daily satellite constellation.** (a) Methane-abundant regions and associated super-emitters are captured by
407 the TROPOMI and PRISMA, respectively. Their locations are marked by black rectangles and dots. Their names are obtained
408 from the Google Map, usually being the names of the nearest O&G fields and coal mines. (b ~ g) Each group clarifies a
409 methane-abundant region and explicit super-emitters (b1 ~ b4, c1 ~ c4, d1 ~ d4, e1 ~ e4, f1 ~ f2, and g1 ~ g2). For each super-
410 emitter (five-pointed stars), the overpass moments of the multi-tiered satellite constellation and the consequent emission
411 estimate are presented. Its base map is obtained from the ©Google Map. The second color bar for the PRISMA is suitable
412 for the super-emitters in China, while the first is for other countries.



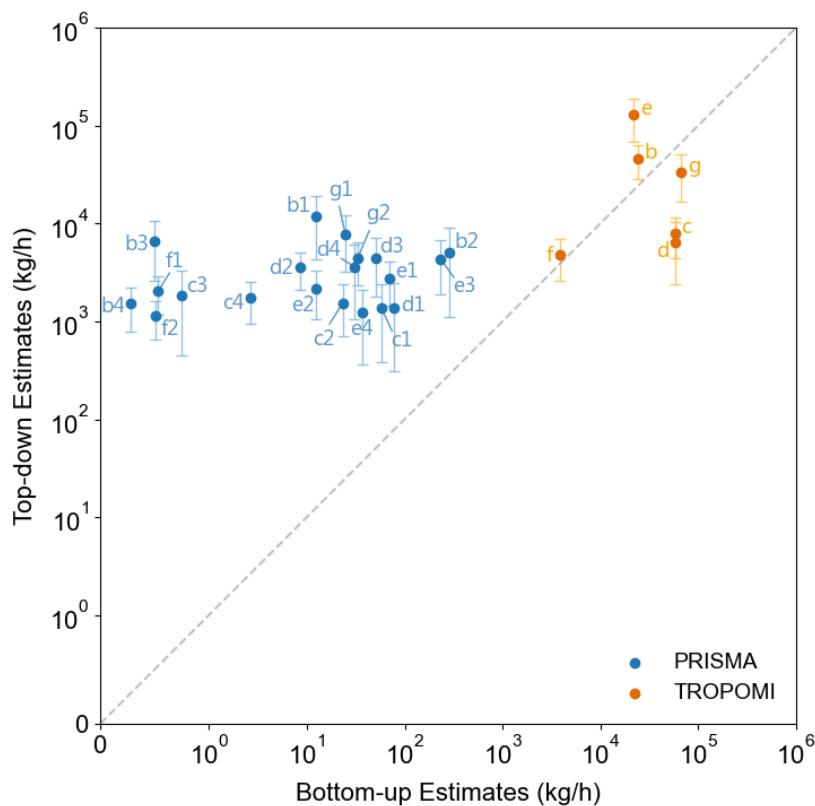
413

414 **Fig. 2. High contributions of methane super-emitters to corresponding regional methane budgets.**



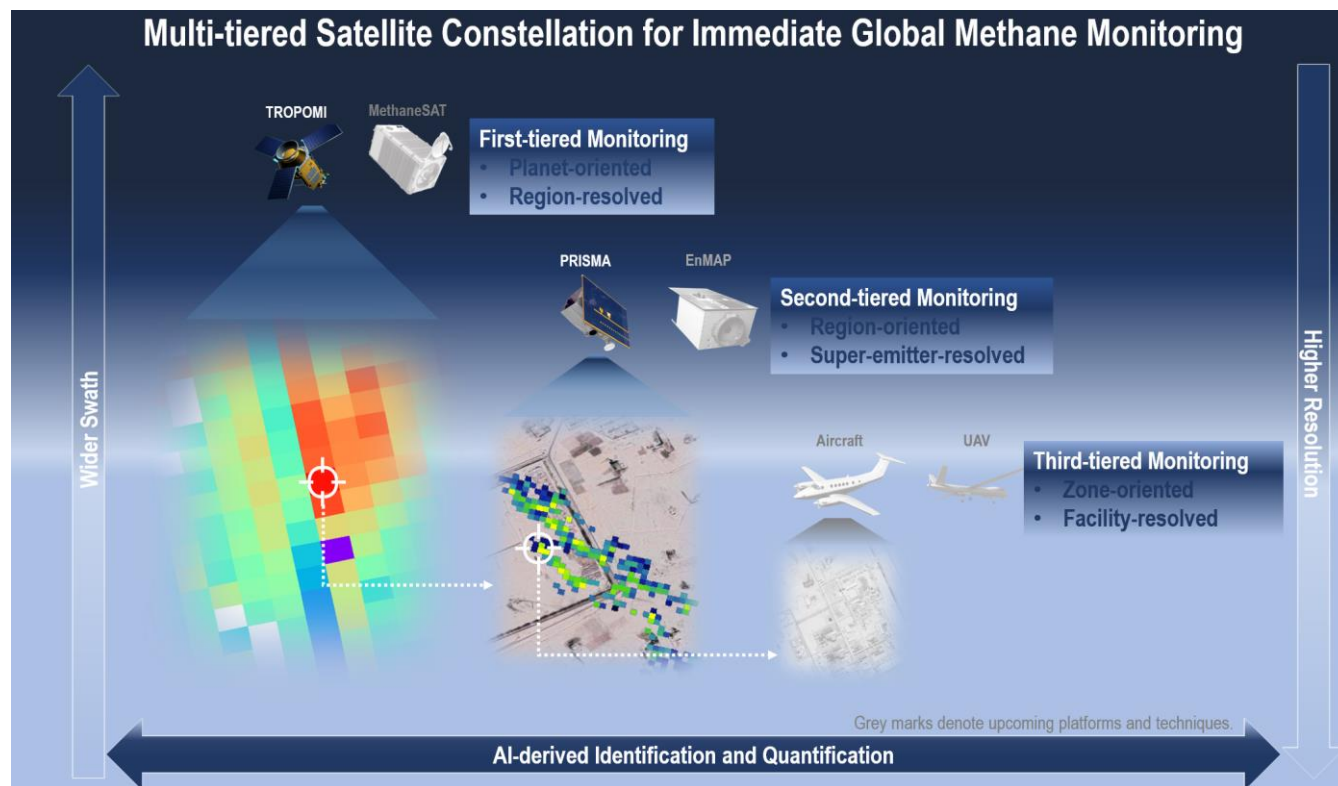
415

416 **Fig. 3. Comparison of emission estimates of methane plumes between surveys.** The surveys for the California field and
417 Permian basin are selected as the references. They report 1181 and 39 methane plumes, while our second-tiered survey attempts
418 29 plumes. Violin plots show statistical distributions of methane plume emission rates for these surveys. For each survey, the
419 grey dots refer to the emission rates of the individual plumes and the red dot represents the median value.



420

421 **Fig. 4. Multi-tiered emission estimates versus bottom-up emission inventories.** We first interpolate the bottom-up emission
422 inventories into the resolution consistent with our multi-tiered results. On this basis, the bottom-up emission rates in the grids
423 that the detected hotspots and plumes cover are summed up to compare with the results. The detected hotspots (yellow dots)
424 and plumes (blue dots) correspond to those as shown in Fig. 1. The grey dashed line represents the ratio of the bottom-up
425 emissions to the top-down ones of 1:1.



426

427 **Fig. 5. Multi-tiered satellite framework for immediate global methane monitoring.** This framework harmonizes global-
428 scale and high-resolution methane retrievals, with a dual focus on mapping region-scale and plant-level drivers. In this work,
429 the framework reconciles the spacious swath of TROPOMI (i.e., ~ 2600 km) with the high resolution of PRISMA (i.e., 30 ×
430 30 m²), in contrast to conventional satellite-based surveys that were of either insufficient samplings or narrow views. Looking
431 forward, developments of Earth's monitoring platforms (e.g., satellites, aircrafts, and unmanned drones) and artificial
432 intelligence will continue to strengthen the performance of methane plume retrievals and emission estimates. On eve of the
433 Paris target, at least while a super methane satellite with spacious swath, high resolution, and agile analysis is not in place, our
434 multi-tiered satellite constellation has important implications for measuring global methane pledges. The appearances of the
435 TROPOMI, MethaneSAT, PRISMA, and EnMAP are obtained from <http://www.tropomi.eu/>, <https://www.methanesat.org>,
436 <https://www.asi.it/en/earth-science/prisma/>, and <https://www.enmap.org/>, respectively. The methane maps from the
437 TROPOMI and PRISMA refer to the results in Figs. 1e and 1b1. The grey marks indicate upcoming platforms (i.e.,
438 MethaneSAT and EnMAP) and techniques (e.g., AI techniques that can optimize the identification and quantification of
439 methane super-emitters).

440



441 **Data availability.**

442 The operational TROPOMI product is available at <https://scihub.copernicus.eu/>, <https://www.temis.nl/emissions/data.php>. The
443 PRISMA data are publicly available to registered users at <https://prisma.asi.it/>. The WRF-CHEM model code is available at
444 <https://ruc.noaa.gov/wrf/wrf-chem/>. All Sentinel-2 satellite data are publicly available through the Copernicus Open Access
445 Hub (<https://scihub.copernicus.eu/>). The HITRAN line spectra is publicly available through the HITRANonline database
446 (<https://hitran.org/>). The ERA5 data come from <https://www.ecmwf.int/en/forecasts/datasets/reanalysis-datasets/era5>. The
447 EDGARv6.0 dataset comes from <https://edgar.jrc.ec.europa.eu/gallery?release=v60ghg&substance=CH4§or=TOTALS>.

448 **Code availability.**

449 The codes are available upon request to corresponding author.

450 **Supplementary information.**

451 Supplementary information accompanies this paper.

452 **Author contributions.**

453 P. L. designed this study and wrote the manuscript. P. L. and Y. W. developed the retrieval algorithm. P. L., Y. W., X. G., Y.
454 H., and Y. P. performed the data analysis. S. Y., A.B., D. R., and J. H. S. contributed to the manuscript.

455 **Competing interests.**

456 The authors declare no competing interests.

457 **Acknowledgements.**

458 We thank ESA and the S-5P/TROPOMI team for the great work on initiating and realizing TROPOMI data. We also thank
459 the Italian Space Agency for the great work on the PRISMA data. This study is supported by National Natural Science
460 Foundation of China (No. 22006030, 22076172, 21577126 and 41561144004), Science and Technology Program of Hebei
461 Province (22343702D), Hebei Youth Top Fund (BJ2020032), Research Foundation of Education Bureau of Hebei
462 (QN2019184), Basic Scientific Research Foundation of Hebei (KY2021024), Initiation Fund of Hebei Agricultural University
463 (412201904 and YJ201833), the Department of Science and Technology of China (No. 2016YFC0202702, 2018YFC0213506
464 and 2018YFC0213503), and National Research Program for Key Issues in Air Pollution Control in China (No. DQGG0107).



465 References

- 466 A., A. R., Daniel, Z.-A., R., L. D., T., A. D., R., B. Z., R., B. A., J., D. K., C., H. S., J., J. D., Anna, K., A., K. E., K., L. B.,
467 Thomas, L., D., M. J., J., M. A., Mark, O., W., P. S., Jeff, P., L., R. A., B., S. P., Colm, S., Amy, T.-S., C., W. S. and P., H.
468 S.: Assessment of methane emissions from the U.S. oil and gas supply chain, *Science* (80-.), 361(6398), 186–188,
469 doi:10.1126/science.aar7204, 2018.
- 470 A., F. A., C., I. G., E., C. L., A., E. J., E., H. N., C., M. H., Joeri, R., Reed, S., Jameel, A., R., A. G., Jared, C., Minji, J.,
471 James, M., Anupriya, M. and Wenjing, S.: Can Paris pledges avert severe climate change?, *Science* (80-.), 350(6265),
472 1168–1169, doi:10.1126/science.aad5761, 2015.
- 473 Allen, D. T., Torres, V. M., Thomas, J., Sullivan, D. W., Harrison, M., Hendler, A., Herndon, S. C., Kolb, C. E., Fraser, M.
474 P., Hill, A. D., Lamb, B. K., Miskimins, J., Sawyer, R. F. and Seinfeld, J. H.: Measurements of methane emissions at natural
475 gas production sites in the United States, *Proc. Natl. Acad. Sci.*, 110(44), 17768 LP – 17773, doi:10.1073/pnas.1304880110,
476 2013.
- 477 Alvarez, R. A., Zavala-Araiza, D., Lyon, D. R., Allen, D. T., Barkley, Z. R., Brandt, A. R., Davis, K. J., Herndon, S. C.,
478 Jacob, D. J. and Karion, A.: Assessment of methane emissions from the US oil and gas supply chain, *Science* (80-.),
479 361(6398), 186–188, 2018.
- 480 Butz, A., Hasekamp, O. P., Frankenberg, C. and Aben, I.: Retrievals of atmospheric CO₂ from simulated space-borne
481 measurements of backscattered near-infrared sunlight: accounting for aerosol effects, *Appl. Opt.*, 48(18), 3322–3336,
482 doi:10.1364/AO.48.003322, 2009.
- 483 Butz, A., Guerlet, S., Hasekamp, O., Schepers, D., Galli, A., Aben, I., Frankenberg, C., Hartmann, J.-M., Tran, H., Kuze, A.,
484 Keppel-Aleks, G., Toon, G., Wunch, D., Wennberg, P., Deutscher, N., Griffith, D., Macatangay, R., Messerschmidt, J.,
485 Notholt, J. and Warneke, T.: Toward accurate CO₂ and CH₄ observations from GOSAT, *Geophys. Res. Lett.*, 38(14),
486 doi:https://doi.org/10.1029/2011GL047888, 2011.
- 487 Conley, S., Franco, G., Faloona, I., Blake, D. R., Peischl, J. and Ryerson, T. B.: Methane emissions from the 2015 Aliso
488 Canyon blowout in Los Angeles, CA, *Science* (80-.), 351(6279), 1317–1320, 2016.
- 489 Crippa, M., Solazzo, E., Huang, G., Guizzardi, D., Koffi, E., Muntean, M., Schieberle, C., Friedrich, R. and Janssens-
490 Maenhout, G.: High resolution temporal profiles in the Emissions Database for Global Atmospheric Research, *Sci. Data*,
491 7(1), 121, doi:10.1038/s41597-020-0462-2, 2020.
- 492 Cusworth, D. H., Jacob, D. J., Varon, D. J., Chan Miller, C., Liu, X., Chance, K., Thorpe, A. K., Duren, R. M., Miller, C. E.,
493 Thompson, D. R., Frankenberg, C., Guanter, L. and Randles, C. A.: Potential of next-generation imaging spectrometers to
494 detect and quantify methane point sources from space, *Atmos. Meas. Tech.*, 12(10), 5655–5668, doi:10.5194/amt-12-5655-
495 2019, 2019.



- 496 Cusworth, D. H., Duren, R. M., Yadav, V., Thorpe, A. K., Verhulst, K., Sander, S., Hopkins, F., Rafiq, T. and Miller, C. E.:
497 Synthesis of Methane Observations Across Scales: Strategies for Deploying a Multitiered Observing Network, *Geophys.*
498 *Res. Lett.*, 47(7), e2020GL087869, doi:<https://doi.org/10.1029/2020GL087869>, 2020.
- 499 Cusworth, D. H., Duren, R. M., Thorpe, A. K., Olson-Duvall, W., Heckler, J., Chapman, J. W., Eastwood, M. L.,
500 Helmlinger, M. C., Green, R. O., Asner, G. P., Dennison, P. E. and Miller, C. E.: Intermittency of Large Methane Emitters in
501 the Permian Basin, *Environ. Sci. Technol. Lett.*, 8(7), 567–573, doi:10.1021/acs.estlett.1c00173, 2021a.
- 502 Cusworth, D. H., Duren, R. M., Thorpe, A. K., Pandey, S., Maasackers, J. D., Aben, I., Jervis, D., Varon, D. J., Jacob, D. J.
503 and Randles, C. A.: Multisatellite Imaging of a Gas Well Blowout Enables Quantification of Total Methane Emissions,
504 *Geophys. Res. Lett.*, 48(2), e2020GL090864, 2021b.
- 505 Deng, Z., Ciais, P., Tzompa-Sosa, Z. A., Saunio, M., Qiu, C., Tan, C., Sun, T., Ke, P., Cui, Y., Tanaka, K., Lin, X.,
506 Thompson, R. L., Tian, H., Yao, Y., Huang, Y., Lauerwald, R., Jain, A. K., Xu, X., Bastos, A., Sitch, S., Palmer, P. I.,
507 Lauvaux, T., d’Aspremont, A., Giron, C., Benoit, A., Poulter, B., Chang, J., Petrescu, A. M. R., Davis, S. J., Liu, Z., Grassi,
508 G., Albergel, C., Tubiello, F. N., Perugini, L., Peters, W. and Chevallier, F.: Comparing national greenhouse gas budgets
509 reported in UNFCCC inventories against atmospheric inversions, *Earth Syst. Sci. Data*, 14(4), 1639–1675, doi:10.5194/essd-
510 14-1639-2022, 2022.
- 511 Duren, R. M., Thorpe, A. K., Foster, K. T., Rafiq, T., Hopkins, F. M., Yadav, V., Bue, B. D., Thompson, D. R., Conley, S.
512 and Colombi, N. K.: California’s methane super-emitters, *Nature*, 575(7781), 180–184, 2019.
- 513 Ehret, T., Truchis, A. De, Mazzolini, M., Morel, J.-M., d’Aspremont, A., Lauvaux, T., Duren, R., Cusworth, D. and
514 Facciolo, G.: Global Tracking and Quantification of Oil and Gas Methane Emissions from Recurrent Sentinel-2 Imagery,
515 2021.
- 516 Englander, J. G., Brandt, A. R., Conley, S., Lyon, D. R. and Jackson, R. B.: Aerial Interyear Comparison and Quantification
517 of Methane Emissions Persistence in the Bakken Formation of North Dakota, USA, *Environ. Sci. Technol.*, 52(15), 8947–
518 8953, doi:10.1021/acs.est.8b01665, 2018.
- 519 Etminan, M., Myhre, G., Highwood, E. J. and Shine, K. P.: Radiative forcing of carbon dioxide, methane, and nitrous oxide:
520 A significant revision of the methane radiative forcing, *Geophys. Res. Lett.*, 43(24), 12,612–614,623,
521 doi:<https://doi.org/10.1002/2016GL071930>, 2016.
- 522 Foote, M. D., Dennison, P. E., Thorpe, A. K., Thompson, D. R., Jongaramrungruang, S., Frankenberg, C. and Joshi, S. C.:
523 Fast and Accurate Retrieval of Methane Concentration From Imaging Spectrometer Data Using Sparsity Prior, *IEEE Trans.*
524 *Geosci. Remote Sens.*, 58(9), 6480–6492, doi:10.1109/TGRS.2020.2976888, 2020.
- 525 Frankenberg, C., Thorpe, A. K., Thompson, D. R., Hulley, G., Kort, E. A., Vance, N., Borchardt, J., Krings, T., Gerilowski,
526 K., Sweeney, C., Conley, S., Bue, B. D., Aubrey, A. D., Hook, S. and Green, R. O.: Airborne methane remote measurements
527 reveal heavy-tail flux distribution in Four Corners region, *Proc. Natl. Acad. Sci.*, 113(35), 9734 LP – 9739,
528 doi:10.1073/pnas.1605617113, 2016.



- 529 G., N. E., J., D. E. and Philippe, B.: Methane on the Rise—Again, *Science* (80-.), 343(6170), 493–495,
530 doi:10.1126/science.1247828, 2014.
- 531 Gålfalk, M., Nilsson Påledal, S. and Bastviken, D.: Sensitive Drone Mapping of Methane Emissions without the Need for
532 Supplementary Ground-Based Measurements, *ACS Earth Sp. Chem.*, 5(10), 2668–2676,
533 doi:10.1021/acsearthspacechem.1c00106, 2021.
- 534 Ganesan, A. L., Schwietzke, S., Poulter, B., Arnold, T., Lan, X., Rigby, M., Vogel, F. R., van der Werf, G. R., Janssens-
535 Maenhout, G., Boesch, H., Pandey, S., Manning, A. J., Jackson, R. B., Nisbet, E. G. and Manning, M. R.: Advancing
536 Scientific Understanding of the Global Methane Budget in Support of the Paris Agreement, *Global Biogeochem. Cycles*,
537 33(12), 1475–1512, doi:https://doi.org/10.1029/2018GB006065, 2019.
- 538 Guanter, L., Irakulis-Loitxate, I., Gorroño, J., Sánchez-García, E., Cusworth, D. H., Varon, D. J., Cogliati, S. and Colombo,
539 R.: Mapping methane point emissions with the PRISMA spaceborne imaging spectrometer, *Remote Sens. Environ.*, 265,
540 112671, doi:https://doi.org/10.1016/j.rse.2021.112671, 2021.
- 541 Hasekamp, O. P. and Butz, A.: Efficient calculation of intensity and polarization spectra in vertically inhomogeneous
542 scattering and absorbing atmospheres, *J. Geophys. Res. Atmos.*, 113(D20), doi:https://doi.org/10.1029/2008JD010379, 2008.
- 543 Hersbach, H., Bell, B., Berrisford, P., Hirahara, S., Horányi, A., Muñoz-Sabater, J., Nicolas, J., Peubey, C., Radu, R.,
544 Schepers, D., Simmons, A., Soci, C., Abdalla, S., Abellan, X., Balsamo, G., Bechtold, P., Biavati, G., Bidlot, J., Bonavita,
545 M., De Chiara, G., Dahlgren, P., Dee, D., Diamantakis, M., Dragani, R., Flemming, J., Forbes, R., Fuentes, M., Geer, A.,
546 Haimberger, L., Healy, S., Hogan, R. J., Hólm, E., Janisková, M., Keeley, S., Laloyaux, P., Lopez, P., Lupu, C., Radnoti, G.,
547 de Rosnay, P., Rozum, I., Vamborg, F., Villaume, S. and Thépaut, J.-N.: The ERA5 global reanalysis, *Q. J. R. Meteorol.*
548 *Soc.*, 146(730), 1999–2049, doi:https://doi.org/10.1002/qj.3803, 2020.
- 549 Hoffmann, L., Günther, G., Li, D., Stein, O., Wu, X., Griessbach, S., Heng, Y., Konopka, P., Müller, R., Vogel, B. and
550 Wright, J. S.: From ERA-Interim to ERA5: the considerable impact of ECMWF’s next-generation reanalysis on Lagrangian
551 transport simulations, *Atmos. Chem. Phys.*, 19(5), 3097–3124, doi:10.5194/acp-19-3097-2019, 2019.
- 552 Hu, H., Landgraf, J., Detmers, R., Borsdorff, T., Aan de Brugh, J., Aben, I., Butz, A. and Hasekamp, O.: Toward Global
553 Mapping of Methane With TROPOMI: First Results and Intersatellite Comparison to GOSAT, *Geophys. Res. Lett.*, 45(8),
554 3682–3689, doi:https://doi.org/10.1002/2018GL077259, 2018.
- 555 Itziar, I.-L., Luis, G., Yin-Nian, L., J., V. D., D., M. J., Yuzhong, Z., Apisada, C., C., W. S., K., T. A., M., D. R., Christian,
556 F., R., L. D., Benjamin, H., H., C. D., Yongguang, Z., Karl, S., Javier, G., Elena, S.-G., P., S. M., Kaiqin, C., Haijian, Z.,
557 Jian, L., Xun, L., Ilse, A. and J., J. D.: Satellite-based survey of extreme methane emissions in the Permian basin, *Sci. Adv.*,
558 7(27), eabf4507, doi:10.1126/sciadv.abf4507, 2021.
- 559 Itziar, I.-L., Luis, G., Yin-Nian, L., J., V. D., D., M. J., Yuzhong, Z., Apisada, C., C., W. S., K., T. A., M., D. R., Christian,
560 F., R., L. D., Benjamin, H., H., C. D., Yongguang, Z., Karl, S., Javier, G., Elena, S.-G., P., S. M., Kaiqin, C., Haijian, Z.,
561 Jian, L., Xun, L., Ilse, A. and J., J. D.: Satellite-based survey of extreme methane emissions in the Permian basin, *Sci. Adv.*,
562 7(27), eabf4507, doi:10.1126/sciadv.abf4507, 2022.



563 Jacob, D. J., Turner, A. J., Maasackers, J. D., Sheng, J., Sun, K., Liu, X., Chance, K., Aben, I., McKeever, J. and
564 Frankenberg, C.: Satellite observations of atmospheric methane and their value for quantifying methane emissions, *Atmos.*
565 *Chem. Phys.*, 16(22), 14371–14396, doi:10.5194/acp-16-14371-2016, 2016.

566 Jervis, D., McKeever, J., Durak, B. O. A., Sloan, J. J., Gains, D., Varon, D. J., Ramier, A., Strupler, M. and Tarrant, E.: The
567 GHGSat-D imaging spectrometer, *Atmos. Meas. Tech.*, 14(3), 2127–2140, doi:10.5194/amt-14-2127-2021, 2021.

568 K., S. J., P., S. D., J., M. M. and V., R.: What Role for Short-Lived Climate Pollutants in Mitigation Policy?, *Science* (80-.),
569 342(6164), 1323–1324, doi:10.1126/science.1240162, 2013.

570 Kraut, S., Scharf, L. L. and Butler, R. W.: The adaptive coherence estimator: a uniformly most-powerful-invariant adaptive
571 detection statistic, *IEEE Trans. Signal Process.*, 53(2), 427–438, doi:10.1109/TSP.2004.840823, 2005.

572 Lorente, A., Borsdorff, T., Butz, A., Hasekamp, O., aan de Brugh, J., Schneider, A., Wu, L., Hase, F., Kivi, R., Wunch, D.,
573 Pollard, D. F., Shiomi, K., Deutscher, N. M., Velazco, V. A., Roehl, C. M., Wennberg, P. O., Warneke, T. and Landgraf, J.:
574 Methane retrieved from TROPOMI: improvement of the data product and validation of the first 2 years of measurements,
575 *Atmos. Meas. Tech.*, 14(1), 665–684, doi:10.5194/amt-14-665-2021, 2021.

576 Marchese, A. J., Vaughn, T. L., Zimmerle, D. J., Martinez, D. M., Williams, L. L., Robinson, A. L., Mitchell, A. L.,
577 Subramanian, R., Tkacik, D. S., Roscioli, J. R. and Herndon, S. C.: Methane Emissions from United States Natural Gas
578 Gathering and Processing, *Environ. Sci. Technol.*, 49(17), 10718–10727, doi:10.1021/acs.est.5b02275, 2015.

579 Martin, Van, Damme, Lieven, Clarisse, Simon, Whitburn, Juliette, Hadji-Lazaro and Daniel: Industrial and agricultural
580 ammonia point sources exposed, *Nature*, 2018.

581 Masood, E. and Tollefson, J.: COP26 climate pledges: What scientists think so far, *Nature*, d41586-021-03034-z,
582 doi:10.1038/d41586-021-03034-z, 2021.

583 Mayfield, E. N., Robinson, A. L. and Cohon, J. L.: System-wide and Superemitter Policy Options for the Abatement of
584 Methane Emissions from the U.S. Natural Gas System, *Environ. Sci. Technol.*, 51(9), 4772–4780,
585 doi:10.1021/acs.est.6b05052, 2017.

586 McLinden, C. A., Fioletov, V., Shephard, M. W., Krotkov, N., Li, C., Martin, R. V, Moran, M. D. and Joiner, J.: Space-
587 based detection of missing sulfur dioxide sources of global air pollution, *Nat. Geosci.*, 9(7), 496–500, 2016.

588 Mikaloff, F. S. E. and Hinrich, S.: Rising methane: A new climate challenge, *Science* (80-.), 364(6444), 932–933,
589 doi:10.1126/science.aax1828, 2019.

590 Miller, S. M., Michalak, A. M., Detmers, R. G., Hasekamp, O. P., Bruhwiler, L. M. P. and Schwietzke, S.: China’s coal mine
591 methane regulations have not curbed growing emissions, *Nat. Commun.*, 10(1), 1–8, 2019.

592 National Oceanic and Atmospheric Administration: Increase in atmospheric methane set another record during 2021,
593 [online] Available from: [https://www.noaa.gov/news-release/increase-in-atmospheric-methane-set-another-record-during-](https://www.noaa.gov/news-release/increase-in-atmospheric-methane-set-another-record-during-2021)
594 2021, 2022.



- 595 Nisbet, E. G., Manning, M. R., Dlugokencky, E. J., Fisher, R. E., Lowry, D., Michel, S. E., Myhre, C. L., Platt, S. M., Allen,
596 G. and Bousquet, P.: Very Strong Atmospheric Methane Growth in the 4 Years 2014–2017: Implications for the Paris
597 Agreement, *Global Biogeochem. Cycles*, 33, 2019.
- 598 Nisbet, E. G., Fisher, R. E., Lowry, D., France, J. L., Allen, G., Bakkaloglu, S., Broderick, T. J., Cain, M., Coleman, M.,
599 Fernandez, J., Forster, G., Griffiths, P. T., Iverach, C. P., Kelly, B. F. J., Manning, M. R., Nisbet-Jones, P. B. R., Pyle, J. A.,
600 Townsend-Small, A., al-Shalaan, A., Warwick, N. and Zazzeri, G.: Methane Mitigation: Methods to Reduce Emissions, on
601 the Path to the Paris Agreement, *Rev. Geophys.*, 58(1), e2019RG000675, doi:<https://doi.org/10.1029/2019RG000675>, 2020.
- 602 Ocko, I. B., Sun, T., Shindell, D., Oppenheimer, M., Hristov, A. N., Pacala, S. W., Mauzerall, D. L., Xu, Y. and Hamburg, S.
603 P.: Acting rapidly to deploy readily available methane mitigation measures by sector can immediately slow global warming,
604 *Environ. Res. Lett.*, 16(5), 54042, doi:10.1088/1748-9326/abf9c8, 2021.
- 605 Ouerghi, E., Ehret, T., de Franchis, C., Facciolo, G., Lauvaux, T., Meinhardt, E. and Morel, J.-M.: DETECTION OF
606 METHANE PLUMES IN HYPERSPECTRAL IMAGES FROM SENTINEL-5P BY COUPLING ANOMALY
607 DETECTION AND PATTERN RECOGNITION, *ISPRS Ann. Photogramm. Remote Sens. Spat. Inf. Sci.*, V-3–2021, 81–
608 87, doi:10.5194/isprs-annals-V-3-2021-81-2021, 2021.
- 609 Pandey, S., Gautam, R., Houweling, S., Van Der Gon, H. D., Sadavarte, P., Borsdorff, T., Hasekamp, O., Landgraf, J., Tol,
610 P. and Van Kempen, T.: Satellite observations reveal extreme methane leakage from a natural gas well blowout, *Proc. Natl.*
611 *Acad. Sci.*, 116(52), 26376–26381, 2019.
- 612 Paoletti, M. E., Haut, J. M., Plaza, J. and Plaza, A.: A new deep convolutional neural network for fast hyperspectral image
613 classification, *ISPRS J. Photogramm. Remote Sens.*, 145, 120–147, doi:<https://doi.org/10.1016/j.isprsjprs.2017.11.021>, 2018.
- 614 Phil DeCola and WMO Secretariat: An Integrated Global Greenhouse Gas Information System (IG3IS), [online] Available
615 from: <https://public.wmo.int/en/resources/bulletin/integrated-global-greenhouse-gas-information-system-ig3is>, 2017.
- 616 Reichstein, M., Camps-Valls, G., Stevens, B., Jung, M., Denzler, J., Carvalhais, N. and Prabhat: Deep learning and process
617 understanding for data-driven Earth system science, *Nature*, 566(7743), 195–204, doi:10.1038/s41586-019-0912-1, 2019.
- 618 Sánchez-García, E., Gorroño, J., Irakulis-Loitxate, I., Varon, D. J. and Guanter, L.: Mapping methane plumes at very high
619 spatial resolution with the WorldView-3 satellite, *Atmos. Meas. Tech. Discuss.*, 2021, 1–26, doi:10.5194/amt-2021-238,
620 2021.
- 621 Saunio, M., Bousquet, P., Poulter, B., Peregón, A., Ciais, P., Canadell, J. G., Dlugokencky, E. J., Etiope, G., Bastviken, D.,
622 Houweling, S., Janssens-Maenhout, G., Tubiello, F. N., Castaldi, S., Jackson, R. B., Alexe, M., Arora, V. K., Beerling, D. J.,
623 Bergamaschi, P., Blake, D. R., Brailsford, G., Brovkin, V., Bruhwiler, L., Crevoisier, C., Crill, P., Covey, K., Curry, C.,
624 Frankenberg, C., Gedney, N., Höglund-Isaksson, L., Ishizawa, M., Ito, A., Joos, F., Kim, H.-S., Kleinen, T., Krummel, P.,
625 Lamarque, J.-F., Langenfelds, R., Locatelli, R., Machida, T., Maksyutov, S., McDonald, K. C., Marshall, J., Melton, J. R.,
626 Morino, I., Naik, V., O’Doherty, S., Parmentier, F.-J. W., Patra, P. K., Peng, C., Peng, S., Peters, G. P., Pison, I., Prigent, C.,
627 Prinn, R., Ramonet, M., Riley, W. J., Saito, M., Santini, M., Schroeder, R., Simpson, I. J., Spahni, R., Steele, P., Takizawa,
628 A., Thornton, B. F., Tian, H., Tohjima, Y., Viovy, N., Voulgarakis, A., van Weele, M., van der Werf, G. R., Weiss, R.,



- 629 Wiedinmyer, C., Wilton, D. J., Wiltshire, A., Worthy, D., Wunch, D., Xu, X., Yoshida, Y., Zhang, B., Zhang, Z. and Zhu,
630 Q.: The global methane budget 2000–2012, *Earth Syst. Sci. Data*, 8(2), 697–751, doi:10.5194/essd-8-697-2016, 2016.
- 631 Saunio, M., Stavert, A. R., Poulter, B., Bousquet, P., Canadell, J. G., Jackson, R. B., Raymond, P. A., Dlugokencky, E. J.,
632 Houweling, S., Patra, P. K., Ciais, P., Arora, V. K., Bastviken, D., Bergamaschi, P., Blake, D. R., Brailsford, G., Bruhwiler,
633 L., Carlson, K. M., Carrol, M., Castaldi, S., Chandra, N., Crevoisier, C., Crill, P. M., Covey, K., Curry, C. L., Etiope, G.,
634 Frankenberg, C., Gedney, N., Hegglin, M. I., Höglund-Isaksson, L., Hugelius, G., Ishizawa, M., Ito, A., Janssens-Maenhout,
635 G., Jensen, K. M., Joos, F., Kleinen, T., Krummel, P. B., Langenfelds, R. L., Laruelle, G. G., Liu, L., Machida, T.,
636 Maksyutov, S., McDonald, K. C., McNorton, J., Miller, P. A., Melton, J. R., Morino, I., Müller, J., Murguia-Flores, F., Naik,
637 V., Niwa, Y., Noce, S., O’Doherty, S., Parker, R. J., Peng, C., Peng, S., Peters, G. P., Prigent, C., Prinn, R., Ramonet, M.,
638 Regnier, P., Riley, W. J., Rosentreter, J. A., Segers, A., Simpson, I. J., Shi, H., Smith, S. J., Steele, L. P., Thornton, B. F.,
639 Tian, H., Tohjima, Y., Tubiello, F. N., Tsuruta, A., Viovy, N., Voulgarakis, A., Weber, T. S., van Weele, M., van der Werf,
640 G. R., Weiss, R. F., Worthy, D., Wunch, D., Yin, Y., Yoshida, Y., Zhang, W., Zhang, Z., Zhao, Y., Zheng, B., Zhu, Q., Zhu,
641 Q. and Zhuang, Q.: The Global Methane Budget 2000–2017, *Earth Syst. Sci. Data*, 12(3), 1561–1623, doi:10.5194/essd-12-
642 1561-2020, 2020.
- 643 Schellnhuber, H. J., Rahmstorf, S. and Winkelmann, R.: Why the right climate target was agreed in Paris, *Nat. Clim. Chang.*,
644 6(7), 649–653, doi:10.1038/nclimate3013, 2016.
- 645 Schurer, A. P., Cowtan, K., Hawkins, E., Mann, M. E., Scott, V. and Tett, S. F. B.: Interpretations of the Paris climate target,
646 *Nat. Geosci.*, 11(4), 220–221, doi:10.1038/s41561-018-0086-8, 2018.
- 647 Sha, M. K., Langerock, B., Blavier, J.-F. L., Blumenstock, T., Borsdorff, T., Buschmann, M., Dehn, A., De Mazière, M.,
648 Deutscher, N. M., Feist, D. G., García, O. E., Griffith, D. W. T., Grutter, M., Hannigan, J. W., Hase, F., Heikkinen, P.,
649 Hermans, C., Iraci, L. T., Jeseck, P., Jones, N., Kivi, R., Kumps, N., Landgraf, J., Lorente, A., Mahieu, E., Makarova, M. V.,
650 Mellqvist, J., Metzger, J.-M., Morino, I., Nagahama, T., Notholt, J., Ohyama, H., Ortega, I., Palm, M., Petri, C., Pollard, D.
651 F., Rettinger, M., Robinson, J., Roche, S., Roehl, C. M., Röhlings, A. N., Rousogonous, C., Schneider, M., Shiomi, K., Smale,
652 D., Stremme, W., Strong, K., Sussmann, R., Té, Y., Uchino, O., Velazco, V. A., Vigouroux, C., Vrekoussis, M., Wang, P.,
653 Warneke, T., Wizenberg, T., Wunch, D., Yamanouchi, S., Yang, Y. and Zhou, M.: Validation of methane and carbon
654 monoxide from Sentinel-5 Precursor using TCCON and NDACC-IRWG stations, *Atmos. Meas. Tech.*, 14(9), 6249–6304,
655 doi:10.5194/amt-14-6249-2021, 2021.
- 656 Smith, M. L., Gvakharia, A., Kort, E. A., Sweeney, C., Conley, S. A., Faloona, I., Newberger, T., Schnell, R., Schwietzke, S.
657 and Wolter, S.: Airborne Quantification of Methane Emissions over the Four Corners Region, *Environ. Sci. Technol.*,
658 51(10), 5832–5837, doi:10.1021/acs.est.6b06107, 2017.
- 659 Subramanian, R., Williams, L. L., Vaughn, T. L., Zimmerle, D., Roscioli, J. R., Herndon, S. C., Yacovitch, T. I.,
660 Floerchinger, C., Tkacik, D. S., Mitchell, A. L., Sullivan, M. R., Dallmann, T. R. and Robinson, A. L.: Methane Emissions
661 from Natural Gas Compressor Stations in the Transmission and Storage Sector: Measurements and Comparisons with the
662 EPA Greenhouse Gas Reporting Program Protocol, *Environ. Sci. Technol.*, 49(5), 3252–3261, doi:10.1021/es5060258, 2015.



- 663 Sun, K., Zhu, L., Cady-Pereira, K., Chan Miller, C., Chance, K., Clarisse, L., Coheur, P.-F., González Abad, G., Huang, G.,
664 Liu, X., Van Damme, M., Yang, K. and Zondlo, M.: A physics-based approach to oversample multi-satellite, multispecies
665 observations to a common grid, *Atmos. Meas. Tech.*, 11(12), 6679–6701, doi:10.5194/amt-11-6679-2018, 2018.
- 666 T., L., C., G., M., M., A., d’Aspremont, R., D., D., C., D., S. and P., C.: Global assessment of oil and gas methane ultra-
667 emitters, *Science (80-.)*, 375(6580), 557–561, doi:10.1126/science.abj4351, 2022.
- 668 The European Union’s Copernicus Climate Change Service: Annual summary 2021. [online] Available from:
669 [https://climate.copernicus.eu/sites/default/files/custom-uploads/Annual_summary_2021/C3S-CAMS annual temp data and](https://climate.copernicus.eu/sites/default/files/custom-uploads/Annual_summary_2021/C3S-CAMS_annual_temp_data_and_CO2_2021_press_release_final.pdf)
670 [CO2 2021_press release_final.pdf](https://climate.copernicus.eu/sites/default/files/custom-uploads/Annual_summary_2021/C3S-CAMS_annual_temp_data_and_CO2_2021_press_release_final.pdf), n.d.
- 671 Thompson, D. R., Thorpe, A. K., Frankenberg, C., Green, R. O., Duren, R., Guanter, L., Hollstein, A., Middleton, E., Ong,
672 L. and Ungar, S.: Space-based remote imaging spectroscopy of the Aliso Canyon CH₄ superemitter, *Geophys. Res. Lett.*,
673 43(12), 6571–6578, doi:<https://doi.org/10.1002/2016GL069079>, 2016.
- 674 Thorpe, A. K., Frankenberg, C., Aubrey, A. D., Roberts, D. A., Nottrott, A. A., Rahn, T. A., Sauer, J. A., Dubey, M. K.,
675 Costigan, K. R., Arata, C., Steffke, A. M., Hills, S., Haselwimmer, C., Charlesworth, D., Funk, C. C., Green, R. O.,
676 Lundeen, S. R., Boardman, J. W., Eastwood, M. L., Sarture, C. M., Nolte, S. H., Mccubbin, I. B., Thompson, D. R. and
677 McFadden, J. P.: Mapping methane concentrations from a controlled release experiment using the next generation airborne
678 visible/infrared imaging spectrometer (AVIRIS-NG), *Remote Sens. Environ.*, 179, 104–115,
679 doi:<https://doi.org/10.1016/j.rse.2016.03.032>, 2016.
- 680 Turner, A. J., Frankenberg, C. and Kort, E. A.: Interpreting contemporary trends in atmospheric methane, *Proc. Natl. Acad.*
681 *Sci.*, 116(8), 2805 LP – 2813, doi:10.1073/pnas.1814297116, 2019.
- 682 Tuzson, B., Graf, M., Ravelid, J., Scheidegger, P., Kupferschmid, A., Looser, H., Morales, R. P. and Emmenegger, L.: A
683 compact QCL spectrometer for mobile, high-precision methane sensing aboard drones, *Atmos. Meas. Tech.*, 13(9), 4715–
684 4726, doi:10.5194/amt-13-4715-2020, 2020.
- 685 United Nations: Global methane pledge, [online] Available from: [https://unfccc.int/news/world-leaders-kick-start-](https://unfccc.int/news/world-leaders-kick-start-accelerated-climate-action-at-cop26)
686 [accelerated-climate-action-at-cop26](https://unfccc.int/news/world-leaders-kick-start-accelerated-climate-action-at-cop26), 2021.
- 687 Varon, D., McKeever, J., Jervis, D., Maasackers, J. D., Pandey, S., Houweling, S., Aben, I., Scarpelli, T. and Jacob, D. J.:
688 Satellite Discovery of Anomalously Large Methane Point Sources From Oil/Gas Production, *Geophys. Res. Lett.*, 46,
689 doi:10.1029/2019GL083798, 2019.
- 690 Varon, D. J., Jacob, D. J., McKeever, J., Jervis, D., Durak, B. O. A., Xia, Y. and Huang, Y.: Quantifying methane point
691 sources from fine-scale satellite observations of atmospheric methane plumes, *Atmos. Meas. Tech.*, 11(10), 5673–5686,
692 doi:10.5194/amt-11-5673-2018, 2018.
- 693 Varon, D. J., Jacob, D. J., Jervis, D. and McKeever, J.: Quantifying Time-Averaged Methane Emissions from Individual
694 Coal Mine Vents with GHGSat-D Satellite Observations, *Environ. Sci. Technol.*, 54(16), 10246–10253,
695 doi:10.1021/acs.est.0c01213, 2020.



- 696 Varon, D. J., Jervis, D., McKeever, J., Spence, I., Gains, D. and Jacob, D. J.: High-frequency monitoring of anomalous
697 methane point sources with multispectral Sentinel-2 satellite observations, *Atmos. Meas. Tech.*, 14(4), 2771–2785,
698 doi:10.5194/amt-14-2771-2021, 2021.
- 699 Vaughn, T. L., Bell, C. S., Pickering, C. K., Schwietzke, S., Heath, G. A., Pétron, G., Zimmerle, D. J., Schnell, R. C. and
700 Nummedal, D.: Temporal variability largely explains top-down/bottom-up difference in methane emission estimates from a
701 natural gas production region, *Proc. Natl. Acad. Sci.*, 115(46), 11712–11717, 2018.
- 702 Veefkind, J. P., Aben, I., McMullan, K., Förster, H., de Vries, J., Otter, G., Claas, J., Eskes, H. J., de Haan, J. F., Kleipool,
703 Q., van Weele, M., Hasekamp, O., Hoogeveen, R., Landgraf, J., Snel, R., Tol, P., Ingmann, P., Voors, R., Kruizinga, B.,
704 Vink, R., Visser, H. and Levelt, P. F.: TROPOMI on the ESA Sentinel-5 Precursor: A GMES mission for global
705 observations of the atmospheric composition for climate, air quality and ozone layer applications, *Remote Sens. Environ.*,
706 120, 70–83, doi:<https://doi.org/10.1016/j.rse.2011.09.027>, 2012.
- 707 Verhoelst, T., Compornolle, S., Pinardi, G., Lambert, J.-C., Eskes, H. J., Eichmann, K.-U., Fjæraa, A. M., Granville, J.,
708 Niemeijer, S., Cede, A., Tiefengraber, M., Hendrick, F., Pazmiño, A., Bais, A., Bazureau, A., Boersma, K. F., Bognar, K.,
709 Dehn, A., Donner, S., Elokhov, A., Gebetsberger, M., Goutail, F., Grutter de la Mora, M., Gruzdev, A., Gratsea, M., Hansen,
710 G. H., Irie, H., Jepsen, N., Kanaya, Y., Karagkiozidis, D., Kivi, R., Kreher, K., Levelt, P. F., Liu, C., Müller, M., Navarro
711 Comas, M., Piters, A. J. M., Pommereau, J.-P., Portafaix, T., Prados-Roman, C., Puentedura, O., Querel, R., Remmers, J.,
712 Richter, A., Rimmer, J., Rivera Cárdenas, C., Saavedra de Miguel, L., Sinyakov, V. P., Stremme, W., Strong, K., Van
713 Roozendaal, M., Veefkind, J. P., Wagner, T., Wittrock, F., Yela González, M. and Zehner, C.: Ground-based validation of
714 the Copernicus Sentinel-5P TROPOMI NO₂ measurements with the NDACC ZSL-DOAS, MAX-DOAS and Pandonia
715 global networks, *Atmos. Meas. Tech.*, 14(1), 481–510, doi:10.5194/amt-14-481-2021, 2021.
- 716 World Meteorological Organization: Global Atmosphere Watch Programme (GAW), [online] Available from:
717 <https://community.wmo.int/activity-areas/gaw>, 2022.
- 718 Yang, X., Ye, Y., Li, X., Lau, R. Y. K., Zhang, X. and Huang, X.: Hyperspectral Image Classification With Deep Learning
719 Models, *IEEE Trans. Geosci. Remote Sens.*, 56(9), 5408–5423, doi:10.1109/TGRS.2018.2815613, 2018.
- 720 Yu, S., Jia, S. and Xu, C.: Convolutional neural networks for hyperspectral image classification, *Neurocomputing*, 219, 88–
721 98, doi:<https://doi.org/10.1016/j.neucom.2016.09.010>, 2017.
- 722 Yuan, Q., Shen, H., Li, T., Li, Z., Li, S., Jiang, Y., Xu, H., Tan, W., Yang, Q., Wang, J., Gao, J. and Zhang, L.: Deep
723 learning in environmental remote sensing: Achievements and challenges, *Remote Sens. Environ.*, 241, 111716,
724 doi:<https://doi.org/10.1016/j.rse.2020.111716>, 2020.
- 725 Zavala-Araiza, D., Lyon, D., Alvarez, R. A., Palacios, V., Harriss, R., Lan, X., Talbot, R. and Hamburg, S. P.: Toward a
726 Functional Definition of Methane Super-Emitters: Application to Natural Gas Production Sites, *Environ. Sci. Technol.*,
727 49(13), 8167–8174, doi:10.1021/acs.est.5b00133, 2015.



728 Zavala-Araiza, D., Alvarez, R. A., Lyon, D. R., Allen, D. T., Marchese, A. J., Zimmerle, D. J. and Hamburg, S. P.: Super-
729 emitters in natural gas infrastructure are caused by abnormal process conditions, Nat. Commun., 8(1), 14012,
730 doi:10.1038/ncomms14012, 2017.

731 Zhang, M., Li, W. and Du, Q.: Diverse Region-Based CNN for Hyperspectral Image Classification, IEEE Trans. Image
732 Process., 27(6), 2623–2634, doi:10.1109/TIP.2018.2809606, 2018.

733

734